Advanced Materials

ADVANCED MATERIALS
www.advmat.de

RESEARCH ARTICLE

Electrostatic Enhanced Dual-Mode Electronic Skin for Multifunctional Robotic Hands Capable of Object Shape and Material Recognition

Kunwei Bao[1] | Yaguang Guo[2] | Nan Li[1] | Liwu Liu[1,3] | Yanju Liu[1] | Jinsong Leng[4]

[1]Department of Astronautical Science and Mechanics, Harbin Institute of Technology, Harbin, P. R. China | [2]School of Materials Science and Engineering, Harbin Institute of Technology (Shenzhen), Shenzhen, P. R. China | [3]Suzhou Research Institute, Harbin Institute of Technology, Suzhou, P. R. China | [4]Center For Composite Materials and Structures, Science Park of Harbin Institute of Technology, Harbin, P. R. China

Correspondence: Liwu Liu (liulw@hit.edu.cn) | Yanju Liu (yj_liu@hit.edu.cn) | Jinsong Leng (lengjs@hit.edu.cn)

Received: 29 October 2025 | **Revised:** 26 January 2026 | **Accepted:** 2 February 2026

Keywords: dual-mode | electret | electronic skin | non-contact sensing | robotic hand | triboelectric

ABSTRACT

Owing to the increasing requirement for robotic systems to interact intelligently in unstructured and dynamic environments, multimodal perception has become an essential and challenging task. In this study, we introduce a multifunctional robotic hand that can distinguish the shape and material properties of objects using a dual-mode electronic skin (e-skin) capable of non-contact and contact sensing. The e-skin is composed of a polarized expanded polytetrafluoroethylene electret embedded in Ecoflex, thus enabling non-contact sensing via the electrostatic-field effect and contact sensing based on the triboelectric effect. The embedded electret architecture facilitates a high internal charge density, thereby significantly enhancing the intensity and range of non-contact sensing, an advantage not achievable using conventional approaches. Integrating the dual-mode e-skin into a robotic arm endows it with multifunctional capabilities; furthermore, with the assistance of a long short-term memory neural network, the robotic hand achieves 100% and 97.35% accuracies in object-shape and object-material recognition, respectively. This study demonstrates the potential of the proposed e-skin as a versatile multimodal sensing interface for robotic platforms, thereby advancing autonomous and intelligent robotic interactions.

1 | Introduction

Human sensory systems, comprising vision, hearing, touch, smell, and taste, allow interaction with and understanding of the surrounding environment. As robots and advanced automation systems become increasingly prevalent [1–4], the demand for these systems to replicate the human ability to perceive and interact with their surroundings has increased significantly [5–7]. Currently, robotic systems rely primarily on contact-based sensors to gather information [8–14], and recent advances in multifunctional tactile sensing have further expanded their perceptual capabilities. In particular, a variety of multifunctional tactile sensors have been developed that integrate piezoresistive, triboelectric, capacitive, and thermal sensing modalities to extract rich information about contacted objects, such as surface texture, material composition, stiffness, and thermal properties [15–18]. These multifunctional tactile sensing strategies enable robotic systems to achieve more comprehensive and human-like tactile perception when interacting with physical environments. However, relying solely on touch limits the ability of robots to interact with and adapt to unknown environments. Robots should be designed with multimodal sensing capabilities such that they can navigate more effectively in complex and dynamic environments [19–23]. One promising approach is the development of

dual-mode electronic skins (e-skins) that integrate both contact and non-contact sensing, thereby endowing robots with a more comprehensive perception of their surroundings.

Various biological organisms possess evolved non-contact sensing capabilities that allow them to perceive their environment from a distance. Bats perform spatial mapping through ultrasonic echolocation, migratory birds perceive geomagnetic fields for navigation, and insects such as mosquitoes and fruit flies detect humidity gradients to locate hosts or food sources. These diverse biological sensing strategies have inspired a range of non-contact sensing technologies for robotic perception. However, each modality exhibits inherent limitations when translated into practical engineering systems. Ultrasonic sensing relies on active signal emission and is therefore prone to interference from environmental acoustic noise, multipath reflections, and strong material-dependent scattering effects. Geomagnetic sensing, while passive, depends on extremely weak magnetic field variations, making it highly susceptible to electromagnetic interference and challenging to implement reliably in complex environments. In addition, several studies have explored non-contact sensing based on humidity signals [24–26], inspired by insect hygro-reception. Such approaches typically exploit local humidity gradients induced by nearby objects or biological targets. However, humidity-based signals are highly sensitive to ambient airflow, temperature fluctuations, and environmental convection, which can easily distort or mask the weak humidity gradients generated by target objects. As a result, humidity-based non-contact sensing suffers from limited robustness, restricting its applicability in dynamic or uncontrolled environments.

In contrast, some species of fish, such as electric eels and sharks, utilize electroreception to detect the presence of objects or potential prey via electric fields, as illustrated in Figure 1a [27–30]. This method, which relies on electrostatic fields to detect environmental changes, offers greater robustness because electrostatic fields propagate stably and are less susceptible to environmental disturbances. Importantly, electric-field-based non-contact sensing does not rely on the optical, acoustic, or magnetic properties of the target, enabling consistent responses across diverse materials and surface geometries. Therefore, non-contact sensing technology based on electrostatic-field have been developed for robotic applications, with emphasis on establishing an intrinsic electrostatic field within the sensor. Based on their fundamental principles, these sensors can be primarily classified into three categories: systems relying on triboelectric effects [31–37], systems based on ion-electron interactions [38–40], and hybrid systems combining the first two approaches [41, 42]. However, current non-contact sensors present significant limitations owing to the insufficient strength of the intrinsic electrostatic field. The electric-field intensity attenuates rapidly as the distance from the source increases, thereby severely limiting the effective detection range and hindering its full potential for real-world applications. Consequently, the ability to perceive objects from large distances remains a significant challenge. Hence, the strength of the intrinsic electrostatic field must be improved such that its effective range can be extended.

In this study, we propose a dual-mode e-skin for a robotic hand, consisting of pre-polarized expanded polytetrafluoroethylene (ePTFE) embedded in Ecoflex, with silver nanowires (AgNWs) deposited as sensing electrodes on the surface of Ecoflex, as shown in Figure 1b. The e-skin leverages the electrostatic field generated by the embedded ePTFE electret and its intrinsic triboelectric effect to enable both non-contact sensing and contact sensing. The electrostatic field released by an electret originates from its surface charges, which can be generated using various polarization methods, such as corona charging and thermal polarization [43–46]. By adjusting the parameters of these polarization methods and taking other measures, the surface charge density of the electret can be increased, thereby enhancing the electrostatic field, a feature that is not achievable by other non-contact sensing technologies. Consequently, the embedded electret structure in the e-skin enables a larger detection range. This e-skin enables a robotic system to perceive its environment on a larger scale, without requiring direct physical interaction. By integrating this advanced e-skin into robotic hands (Figure 1c), we developed a multifunctional system capable of both non-contact scanning and tactile sensing of objects. This design enables the robotic hand to perform human-like functions analogous to the eyes and hands, integrating long-range perception with physical contact-based exploration (Figure 1d). The acquired data, when processed using machine learning algorithms [47–49], enables an accurate recognition of object shapes and material properties, thereby enabling more intuitive and efficient interactions between robots and their environments.

2 | Results

2.1 | Design of E-Skin

Inspired by the electroreceptive ampullae of Lorenzini in sharks, which detect weak electric fields in aquatic environments, we developed a bioinspired e-skin capable of both non-contact and contact sensing. This design leverages electric field interactions to detect external objects without physical contact, mimicking the way sharks perceive their surroundings. As an object approaches the e-skin, the potential of the AgNWs electrodes varies, with the potential returning to its original state once the object retreats. Upon direct contact, triboelectric signals are induced on the AgNWs electrodes due to frictional effects, as illustrated in Figure 1e. Due to the distinct differences between these two types of signals, it is possible to distinguish whether the object is approaching or in contact with the e-skin.

The fabrication process begins with embedding the ePTFE membrane into liquid Ecoflex, followed by curing to form a flexible and durable elastomeric matrix. Subsequently, AgNWs are deposited onto the Ecoflex surface to form the reference electrode, as illustrated in Figure 1f. The resulting AgNWs layer forms a dense and well-connected percolation network on the Ecoflex substrate (Figure S1), enabling efficient charge transport and reliable potential sensing. The sheet resistance of the AgNWs electrode is 12.34 Ω sq^{-1}, as measured by the four-point probe method, indicating low resistive loss and high electrical conductivity. Owing to the combination of high conductivity and mechanical compliance, the AgNWs electrode effectively transduces electrostatic potential variations while maintaining flexibility, making it well-suited as the reference electrode in the proposed e-skin system.

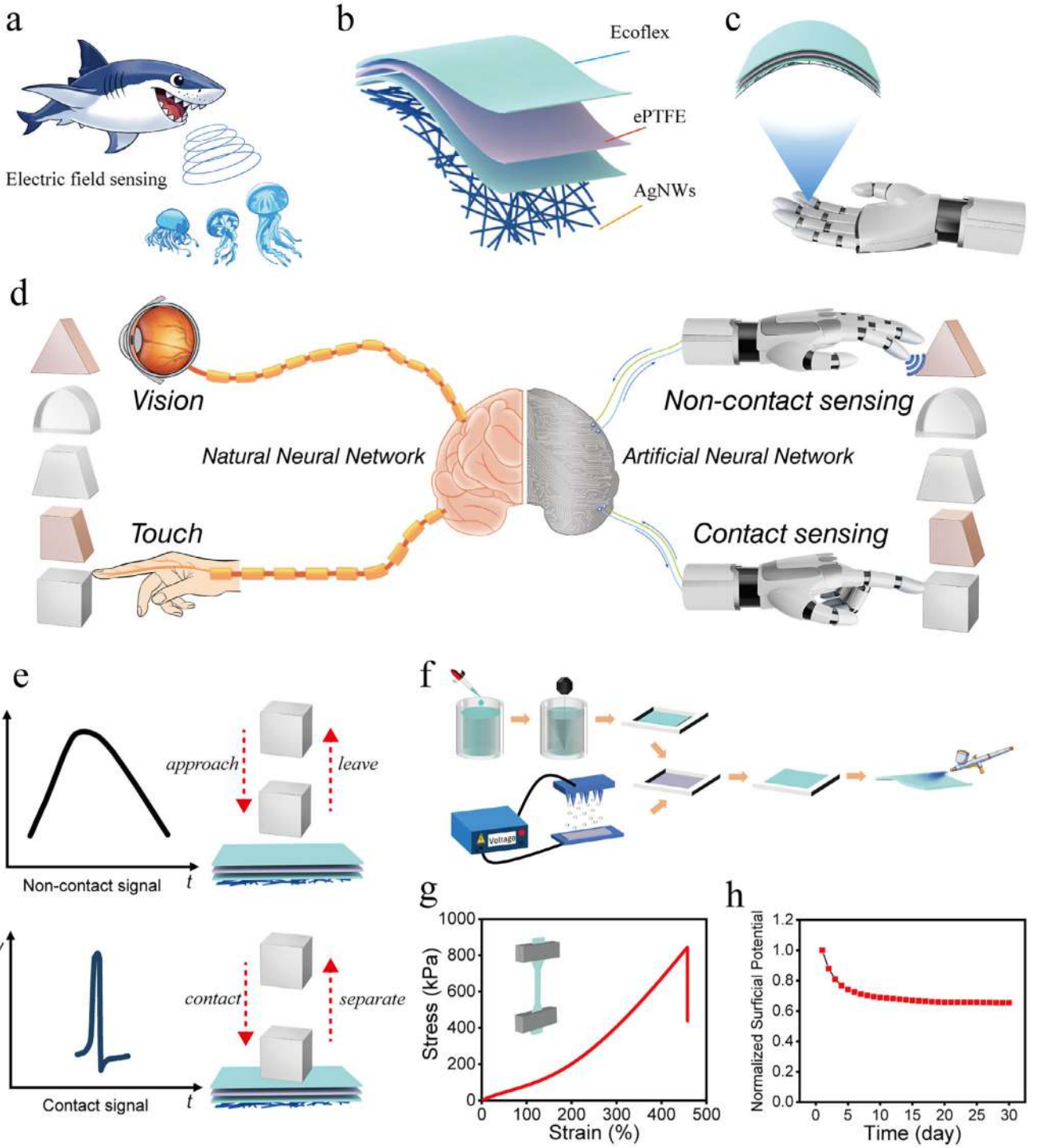

FIGURE 1 | (a) Schematic illustration of electroreceptors in sharks, (b) Structure of e-skin equipped on the robotic hand. (c) A robotic hand equipped with an e-skin. (d) A multifunctional robotic hand exhibiting human-like visual and tactile capabilities. (e) Signals of non-contact sensing and contact sensing. (f) Preparation process of e-skin. (g) Stress–strain curve of e-skin under uniaxial tensile test. (h) Surficial potential variation of e-skin.

The fabricated e-skin is shown in Figure S2 and can withstand tensile strains of up to 450% owing to the high stretchability of the Ecoflex matrix, demonstrating excellent mechanical robustness (Figure 1g). In addition, Ecoflex encapsulation effectively preserves the surface charges of the embedded ePTFE electret, thereby improving its long-term stability. Accordingly, the surface potential of the e-skin remained at ~0.6 of its initial value after one month of storage (Figure 1h), indicating a stable internal electrostatic field that supports sustained non-contact sensing. Immersion tests further confirmed that the encapsulated ePTFE electret retained stable charges after three immersion cycles, whereas an unprotected ePTFE electret lost nearly all charges after a single immersion (Figure S3). These results collectively highlight the durability and reliability of the proposed e-skin in complex environments.

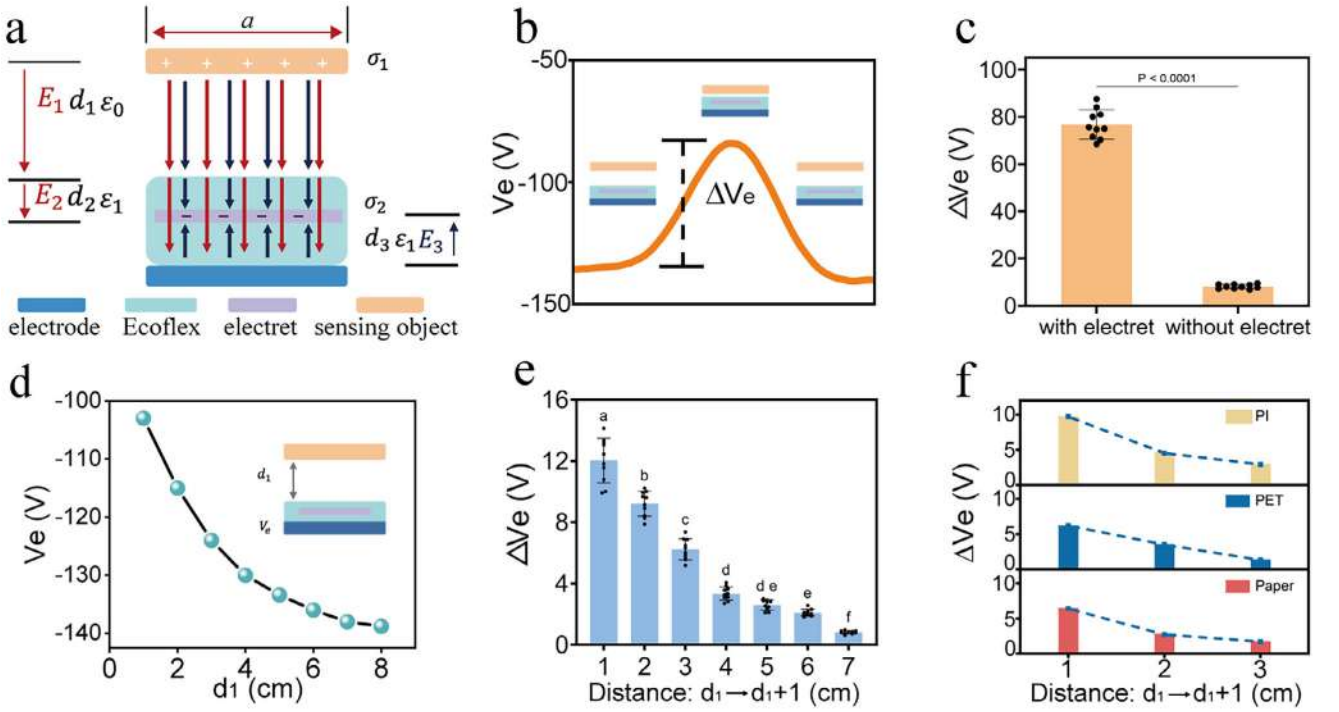

FIGURE 2 | (a) Simplified physical model of non-contact sensing. (b) Electrode potential change ΔV_e due to changes in distance d_1 between sensing object and e-skin. (c) Comparison of ΔV_e in e-skin with and without electret. (d) Electrode potential V_e curve as sensing object propagates away gradually from e-skin. (e) ΔV_e for each 1 cm distance increment as sensing object propagates farther away. (f) Results of non-contact sensing tests performed on PI, PET, and paper.

2.2 | Mechanism of Non-Contact Sensing

To elucidate the non-contact sensing mechanism of the e-skin, a simplified physical model was developed to simulate its interactions with the surrounding environment. Environmental objects can acquire surface charges through various processes, including friction, direct contact, and exposure to ambient factors such as radiation, temperature, and humidity. These interactions result in some objects carrying positive surface charges, while others carry negative surface charges. As illustrated in Figure 2a, the proposed physical model assumes that the sensing object possesses a net positive charge, whereas the ePTFE layer embedded within the e-skin structure is deliberately polarized to exhibit negative surface charges. The non-contact sensing capability originates from the combined effect of the electrostatic field caused by the polarization of the ePTFE layer inside the e-skin and the electrostatic field associated with the sensing object, as well as the interaction between the two electrostatic fields.

The dynamic variation in the distance parameter d_1 between the sensing object and e-skin modulates the electrostatic interaction between them, thus inducing a responsive shift in the potential of the reference electrode V_e, which constitutes the core mechanism by which the e-skin achieves non-contact sensing. Using Gauss's theorem and Kirchhoff's laws, the electrode potential V_e and the variations in the electrode potential ΔV_e with respect to changes in d_1 were obtained as follows (Note S1):

$$V_e = \frac{\sigma_1 + \sigma_2}{2\varepsilon_0} d_1 + \frac{\sigma_1 + \sigma_2}{2\varepsilon_1} d_2 - \frac{\sigma_1 - \sigma_2}{2\varepsilon_1} d_3 \quad (1)$$

$$\Delta V_e = \frac{\sigma_1 + \sigma_2}{2\varepsilon_0} \Delta d \quad (2)$$

where σ_1 and σ_2 denote the surface charge density of the sensing object and ePTFE electret, respectively; d_1 represents the separation distance between the sensing object and e-skin; d_2 and d_3 correspond to the distances between the ePTFE layer and the upper and lower surfaces of the e-skin, respectively. The permittivity of air and Ecoflex is denoted as ε_0 and ε_1, respectively. Equation (1) provides the expression for V_e, while Equation (2) indicates that d_1 directly affects the electrode potential variation ΔV_e.

Simulations and experiments were conducted to validate the theoretical derivations. In the simulations, the approach of the sensing object toward the e-skin corresponds to a decrease in d_1, thus resulting in an increase in V_e, as illustrated in Figure S4. In practical environments, the surface charge distribution of objects is typically non-uniform. To ensure a uniform surface charge distribution in the experiment, corona-polarized PTFE materials were used as the sensing objects. As expected, variations in d_1 caused significant changes in the electrode potential V_e. Specifically, when the positively polarized PTFE approached the e-skin, V_e increased, whereas when it propagated away from the e-skin, V_e decreased. The curve of V_e, as shown in Figure 2b, exhibited a trend consistent with the simulation results and aligned well with the theoretical derivation.

Further comparative experiments were conducted to assess the role of the ePTFE layer in enhancing non-contact sensing. When

testing Ecoflex without an embedded ePTFE electret, the ΔV_e during the approach and withdrawal of the palm remained below 10 V. However, when an e-skin incorporating a polarized ePTFE electret with a surface potential of −2000 V was tested, ΔV_e increased significantly to approximately 80 V, as shown in Figure 2c. This significant enhancement aligns well with the prediction of Equation (2), where ΔV_e is attributed to changes in d_1. Specifically, the magnitude of ΔV_e is proportional to $\frac{\sigma_1+\sigma_2}{2\varepsilon_0}$, thus indicating that the embedded ePTFE electret introduces additional surface charge, thereby enhancing the non-contact sensing capability of the e-skin. This substantial improvement underscores the critical role of the ePTFE electret in increasing the sensing sensitivity and extending the detection range.

The distance-dependent behavior of non-contact sensing was further analyzed by observing the response of a positively polarized PTFE film (surface potential of 1 kV) propagating away from the e-skin, which comprised an embedded ePTFE layer with a surface potential of −1 kV. As shown in Figure 2d, V_e decreased as d_1 increases. The corresponding variation curves reveal that the magnitude of ΔV_e diminished as d_1 between the sensing object and e-skin increased. To quantify this trend, the magnitude of ΔV_e at different distances was plotted (Figure 2e), which illustrates the variation as the sensing object propagated 1 cm farther at each step from an initial distance of 1 cm to a final distance of 7 cm. Specifically, when the sensing object was propagated 1 cm farther from an initial distance of 1 cm, ΔV_e was approximately 10 V. However, as the distance increased, when the sensing object moved 1 cm farther from a distance of 7 cm, ΔV_e diminished gradually, and reduced to approximately 1 V. The tests conducted on oppositely polarized PTFE films yielded consistent results, as shown in Figure S5. This observation highlights a fundamental limitation of non-contact sensing: the sensitivity decreases as the separation distance increases.

The gradual change in ΔV_e deviates from Equation (2) because the equation is derived under the assumption of an ideal infinite parallel plate capacitor, where electric field lines remain perpendicular to the plates, and the field strength depends solely on the surface charge density and dielectric constant. However, when d_1 is comparable to or greater than a (the side length of the e-skin and sensing objects), the finite-size effect of the film becomes significant. In this case, the electric field distribution is no longer uniform and is governed by edge effects. Considering size effects, the variation in ΔV_e with respect to the change in d_1 (Δd) is derived as follows (Note S2):

$$\Delta V_e \approx -\frac{(\sigma_1+\sigma_2)\,a^3}{\varepsilon_0}\frac{\Delta d}{d_1^3} \tag{3}$$

where a represents the side length of the sensing object and e-skin. Equation (3) indicates that as the d_1 between the sensing object and e-skin increases, the same displacement Δd results in a smaller variation in ΔV_e. This relationship underscores the diminishing sensitivity of the system at larger distances, which is a critical factor in the design of non-contact sensing applications.

To further validate this behavior, the non-contact sensing performance was investigated for sensing objects composed of different materials, including polyimide (PI), polyethylene terephthalate (PET), and paper. These materials, which are commonly encountered in daily environments, were selected to simulate real-world objects in practical sensing applications. Consistent with the findings obtained for PTFE films, the sensitivity of non-contact sensing decreased as the distance between these materials and the e-skin increased (Figure 2f). This trend persisted across all the tested materials, with the magnitude of ΔV_e diminishing at greater distances. These results highlight the inherent limitation of non-contact sensing in maintaining high sensitivity over extended distances, thus emphasizing the necessity for optimization in practical implementations.

2.3 | Electrostatic Enhanced Non-Contact Sensing

Based on the analysis above, edge effects in an electric-field distribution must be considered when evaluating ΔV_e in a finite-area parallel-plate system. Thus, key factors affecting the electrode potential change in Equation (3). Among the factors, the surface charge density of both the ePTFE layer in the e-skin and the sensing object, as well as their respective surface areas, are crucial in determining the non-contact sensing performance. By optimizing these parameters, the sensitivity and range of non-contact sensing can be effectively enhanced.

To validate this framework, experimental investigations were conducted to assess the role of surface charge density. By increasing the surface charge density of the ePTFE layer and sensing object, the electric-field intensity is amplified, thus directly improving the non-contact sensing capability. For electrets, the surface charge density is directly proportional to the surface potential, which allows the surface potential to serve as an indicator of the surface charge density. The relationship between the electret's surface potential and surface charge density is derived as follows (Note S3):

$$V_s = U = -\frac{\sigma_2 d_e}{\varepsilon_e} \tag{4}$$

where V_s is the surface potential of the electret; and $-\sigma_2$ represents the surface charge density of the electret, with the negative sign reflecting the polarity of the surface charge on the electret. The thickness and permittivity of the electret are denoted as d_e and ε_e, respectively. Equation (4) expresses the relationship between the surface potential and surface charge density of the electret. During corona polarization, a metal mesh electrode was positioned directly above the PTFE electret, which effectively homogenized the local electric field in the charging region and promoted spatially uniform charge deposition across the electret surface (Figure S6). As a result, the measured surface potential exhibited negligible spatial variation, validating the assumption of uniform surface charge distribution and thereby supporting the linear relationship expressed in Equation (4).

Based on this relationship, experiments were conducted using ePTFE films with surface potentials ranging from −1 to −8 kV, paired with PTFE sensing objects polarized from +1 to +8 kV. During testing, the sensing object was shifted from 1 to 2 cm away from the e-skin, and the corresponding change in the electrode potential was measured as an indicator of the non-contact sensing intensity. A greater ΔV_e signifies stronger non-contact sensing

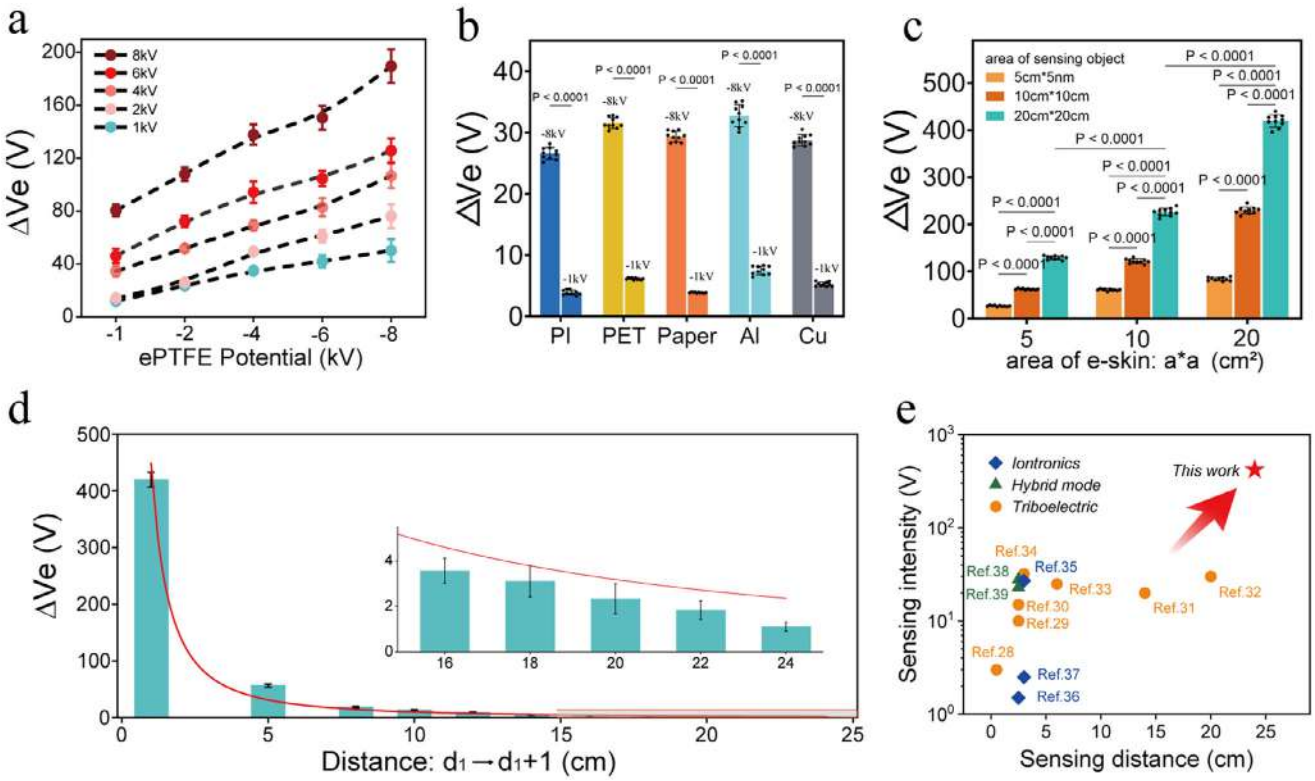

FIGURE 3 | (a) Electrode potential change ΔV_e as a function of surface potential of ePTFE in e-skin and surface potential of sensing object. (b) ΔV_e of various materials under non-contact sensing tests based on surface potentials of ePTFE in e-skin of −8 and −1 kV. (c) Effect of different e-skins and sensing object areas on ΔV_e. (d) Variation trend of ΔV_e when surface potentials of ePTFE and sensing object are −8 and 8 kV, respectively, with both measuring 20 cm × 20 cm. (e) Comparisons of sensing intensity and sensing distance across different non-contact sensing technologies.

capability and suggests an extended sensing range. As shown in Figure 3a, the results clearly show that ΔV_e, which represents the sensing intensity, increased with the surface potentials of both the ePTFE layer and the sensing object. These findings highlight the critical role of surface charge density in enhancing non-contact sensing performance and provide a basis for further optimization.

To further investigate the effect of surface charge density on non-contact sensing performance, additional experiments were conducted using e-skins comprising ePTFE layers with surface potentials of −8 and −1 kV. Various sensing materials, including PI, PET, paper, Al, and Cu, were tested to evaluate the sensing intensity. Each material was initially positioned 1 cm away from the e-skin and then shifted incrementally to 2 cm, while the corresponding ΔV_e values were recorded (see Figure 3b). The results confirmed that increasing the surface charge density of the ePTFE layer significantly enhanced the sensing intensity. For all tested materials, the ΔV_e was substantially higher when the ePTFE surface potential increased from −1 to −8 kV. This finding further validates that increasing the surface charge density of both the e-skin and sensing objects effectively extends the range of non-contact sensing. By employing this method, the e-skin achieves enhanced sensing capabilities over a greater distance, thereby addressing the key limitation of existing non-contact sensing technologies.

In addition to the surface charge density, the surface areas of both the e-skin and sensing object significantly affect the non-contact sensing intensity. When the areas of the sensing object and e-skin increased, the relative contribution of the edge effects diminished, and the electric-field distribution of the system approached that of an ideal uniform field. Consequently, the effective electric-field strength increased, thus resulting in a larger ΔV_e for the same d_1 and Δd. To investigate this effect, experiments were conducted using the e-skin and sensing objects measuring 5 cm × 5 cm, 10 cm × 10 cm, and 20 cm × 20 cm. As shown in Figure 3c, the sensing intensity increased with the surface area.

Based on the results above, we further examined the combined effects of enhancing both the surface charge density and surface area. When the surface potential of the ePTFE layer was set to −8 kV, and the PTFE sensing object was polarized to +8 kV, the system exhibited high sensing intensity and an extended sensing range when both the e-skin and sensing object measured 20 cm × 20 cm. As depicted in Figure 3d, when the PTFE sensing object propagated away from the e-skin in 1 cm increments, beginning from an initial distance of 1 cm, ΔV_e was approximately 400 V initially. As the distance increased, ΔV_e decreased gradually; however, even at a distance of 24 cm, a measurable ΔV_e of approximately 1 V potential was observed. The fitted curve (red line in Figure 3d) further validates the consistent trend of diminishing ΔV_e with increasing distance, thus underscoring the effectiveness of these combined strategies.

As illustrated in Figure 3e, compared with previous non-contact sensing technologies, the simultaneous enhancement of the surface charge density and sensing area significantly improved

both the sensing intensity and range. These results highlight a robust and effective strategy for advancing non-contact sensing performance beyond current limitations.

2.4 | Object-Shape Recognition Based on Non-Contact Sensing

When the e-skin scans objects of different shapes in a non-contact manner, the reference electrode generates distinct signals corresponding to each shape. Object shape can be effectively identified by extracting the characteristic features of the signals and applying machine-learning algorithms. In this study, five representative geometries, cube, triangular prism, semicylinder, right-angled trapezoid, and isosceles trapezoid, were selected to validate this approach.

As illustrated in Figure 4a, when a cube is scanned, its upper surface is generally closer to the e-skin as compared with the cases of other shapes; in this case, the short distance enhances the signal strength owing to charge-aggregation effects. Additionally, the larger top surface area of the cube contributes to a longer signal duration. By contrast, the objects of other shapes exhibit weaker and shorter signal responses, as their curved or slanted surfaces create a more dispersed electric-field distribution. The corresponding signal waveforms for these five shapes are presented in Figure 4b, which shows distinct differences in the signal amplitude and duration.

To enable an accurate classification of the object shapes, feature extraction must be performed to transform raw signals into meaningful features for machine learning. As the signals obtained from object scanning are waveform data, the Fourier transform is employed to convert time-domain waveforms into frequency-domain data. This is because the Fourier transform decomposes complex time-domain signals into sinusoidal components at different frequencies, which renders the primary characteristics of the signal represented more intuitively in the frequency domain, thereby facilitating the extraction of relevant features.

The complete feature-extraction process is shown in Figure 4c. Initially, the waveform data were extended to ensure periodicity in the time domain (Figure 4d). This step is essential for accurate frequency-domain analysis because maintaining periodic continuity enhances the identification of frequency components during the transformation. Subsequently, the DC component is removed, thereby enhancing the prominence of the frequency-domain features by eliminating baseline shifts. Next, the Fourier transform is applied, and five key parameters, average amplitude, amplitude standard deviation, maximum amplitude, and the frequency corresponding to the maximum amplitude and frequency bandwidth, are extracted as input features for machine learning. These features provide a comprehensive representation of the signal's spectral characteristics, which are essential for distinguishing different object shapes.

Following feature extraction, an LSTM neural network is used for classification. LSTM networks are particularly suitable for this task because of their ability to capture long-range temporal dependencies and sequential correlations within the extracted signal features. The LSTM neural network comprises two layers with 64 and 32 time steps, followed by a dense layer that outputs the classification result (see Figure 4e). As shown in Figure 4f, the LSTM model successfully classified the five object shapes, cube, triangular prism, semicylinder, right-angled trapezoid, and isosceles trapezoid, with an accuracy of 100%, and the training process for the LSTM model is shown in Figure 4g. Additionally, convolutional neural networks (CNN) and support vector machines (SVM) were used to process the extracted features for object-shape classification, where 100% and 97.5% accuracies were achieved, respectively, as shown in Figure 4h and Figure S7.

2.5 | Object-Material Recognition Based on Contact Sensing

Contact-based sensing was employed to distinguish various materials by analyzing the triboelectric signals generated during direct physical interaction between the robotic hand and different objects (Figure 5a,b). When the e-skin establishes contact with a material, charge transfer occurs between the surfaces; the direction and magnitude of this transfer are governed by the electronegativity of the material. This process generates triboelectric signals characterized by distinct peak and valley features, which are extracted as signal characteristics to identify the material of the object.

To validate the feasibility of identifying object materials using triboelectric signals generated from contact sensing, a diverse set of materials was tested, including metals such as Al and Cu; polymers such as PI, nylon, and acrylic; paper and human skin, which are commonly encountered materials in both industry and daily environments (Figure 5c). As the e-skin establishes contact with these materials, triboelectric signals are generated, as shown in Figure 5d. The peak and valley values of the triboelectric signals were adopted as the primary features (Figure 5e). It should be noted that the amplitude of the triboelectric signals is influenced by the applied contact force, with larger contact forces leading to higher signal amplitudes (Figure S8). To eliminate the interference of contact force variations on material identification, the contact force exerted by the robotic hand was controlled within a limited and stable range during the material recognition experiments. In addition, environmental humidity also affects the triboelectric output, where higher humidity generally results in reduced signal intensity (Figure S9). In practical robotic manipulation and sensing scenarios, material recognition is typically completed within a relatively short time window, during which the environmental humidity can be regarded as quasi-static and thus has a negligible impact on the classification results.

LSTM, CNN, and SVM models configured with the same network architectures, as described in the previous section, were employed to analyze the extracted triboelectric features to identify the material types of the objects. However, owing to the different input-data formats, the structure of the LSTM neural network differed from that in the previous section, as shown in Figure 5f. The feature values of all training and testing set data are shown in Figure 5g. The trained model showed high classification accuracy, with the LSTM model achieving an accuracy of 97.35% (Figure 5h). The training process of the LSTM model is shown in Figure S10. The CNN and SVM models achieved accuracies of 93.79% and 94.74% (Figure 5i; Figure S11), respectively. Based

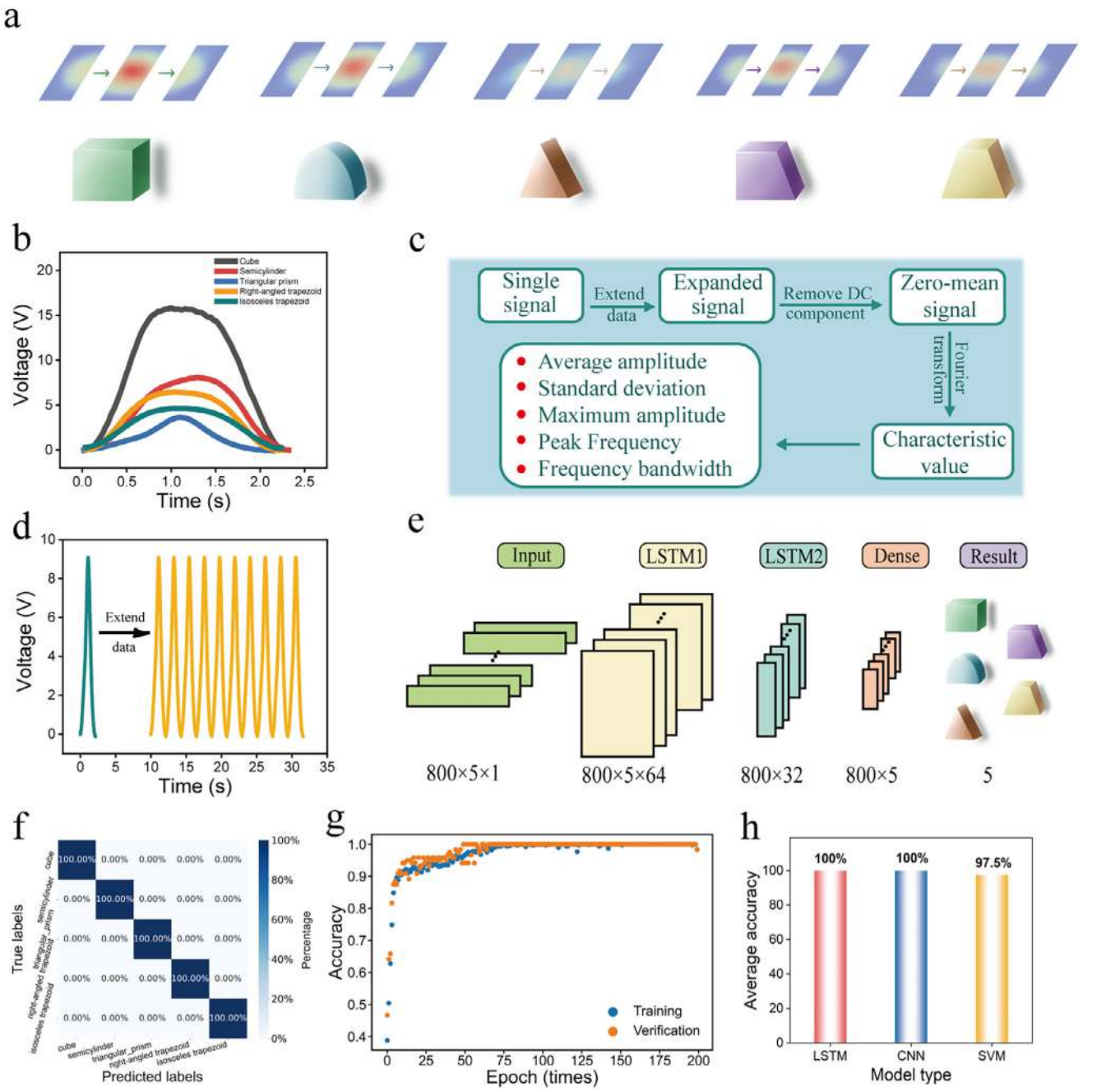

FIGURE 4 | (a) Scanning of objects with different shapes by e-skin. (b) Signals generated by scanning objects of different shapes with e-skin. (c) Complete process of feature extraction. (d) Data extension of waveform. (e) Structure of LSTM model. (f) Confusion matrix for LSTM results in recognizing three different shapes. (g) Training process of LSTM model. (h) Comparison of average accuracies of LSTM, CNN, and SVM models.

on the previous and current sections, the LSTM model exhibited higher accuracy in recognizing object shapes and materials than the CNN and SVM.

2.6 | Demonstration of Multifunctional Robotic Hand

Figure 6a shows the full signal-processing pipeline, in which raw signals are first acquired by the e-skin and then subjected to filtering and analog-to-digital conversion. The processed signals are transmitted to a computer via serial communication, where they are stored and analyzed using an LSTM neural network implemented in Python. The classification results are displayed in real time. To comprehensively assess the capability of the robotic hand equipped with dual-mode e-skin in recognizing both object shapes and materials, a practical demonstration was conducted. The e-skin, which is distinguished by its straightforward fabrication process and structural compatibility, can be easily integrated into a robotic hand using glue, as illustrated in Figure 6b.

To validate the capability of the proposed robotic hand, experiments were conducted to identify the shapes and materials

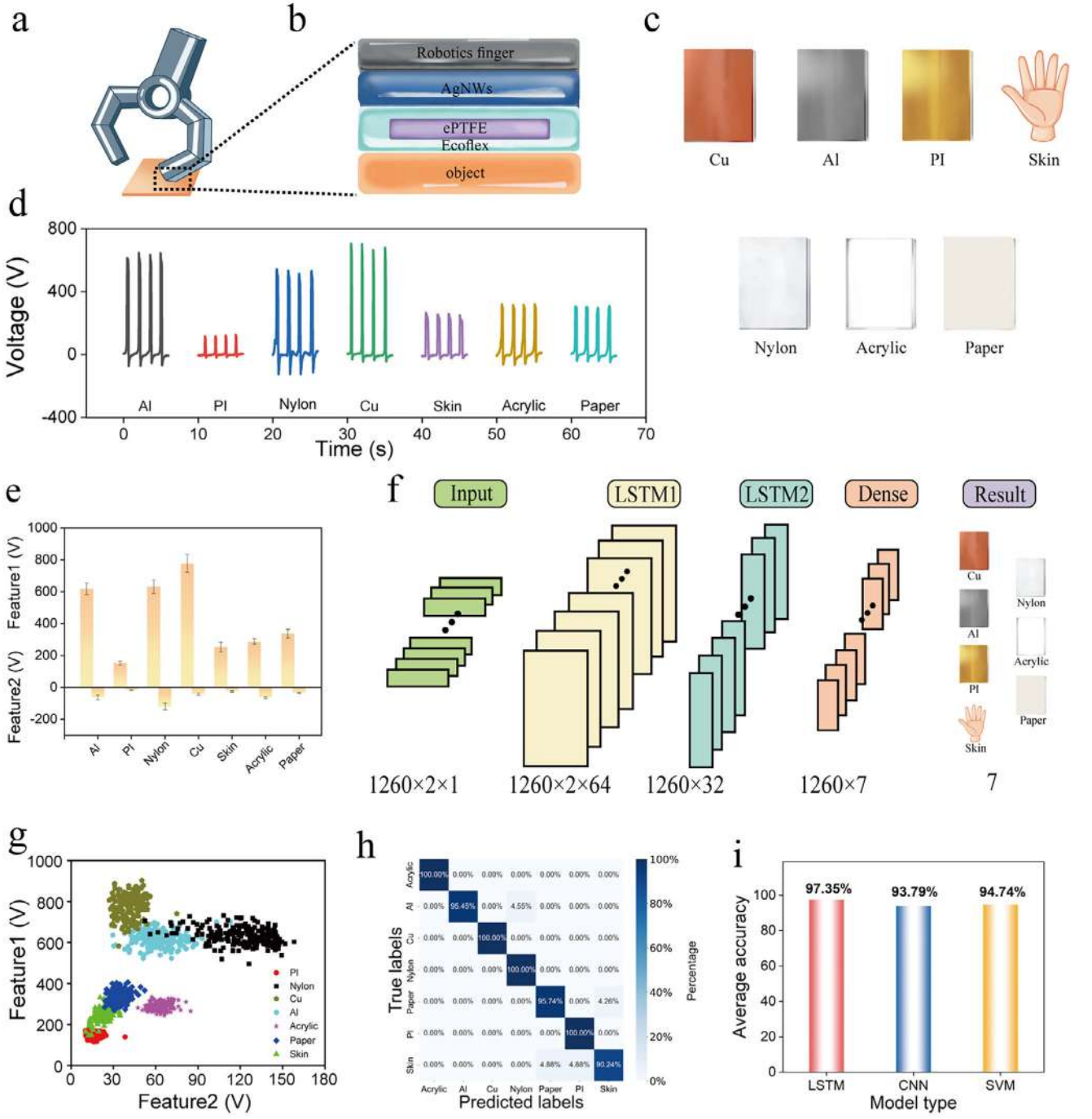

FIGURE 5 | (a, b) Schematic diagram illustrating robotic hand establishing contact with object. (c) Materials tested experimentally. (d) Typical triboelectric signals generated by tested materials. (e) Peak and valley values of triboelectric signals used as feature values. (f) Structure of LSTM model. (g) Feature values derived from training-set data. (h) Confusion matrix of LSTM results for recognizing seven different materials. (i) Comparison of average accuracies of LSTM, CNN, and SVM models.

of various objects. To evaluate the shape-recognition performance, five representative geometries, cube, triangular prism, semicylinder, right-angled trapezoid, and isosceles trapezoid, were fabricated via fused deposition modeling—a 3D printing method. The robotic hand, which was equipped with the e-skin, successfully identified each of these shapes based on the extracted non-contact signal features (Movie S1). Subsequently, the system was tested for material recognition. Seven common materials, PI, Al, nylon, paper, human skin, acrylic, and Cu, were selected. The robotic hand accurately distinguished all seven materials through contact sensing and signal classification (Movie S2), thus demonstrating its effectiveness in material differentiation.

Finally, the capability of the robotic hand for simultaneous shape and material recognition was assessed using composite samples with unique shapes and materials. Specifically, three test objects were used: a semicylindrical acrylic sample, a cubic Al block, a

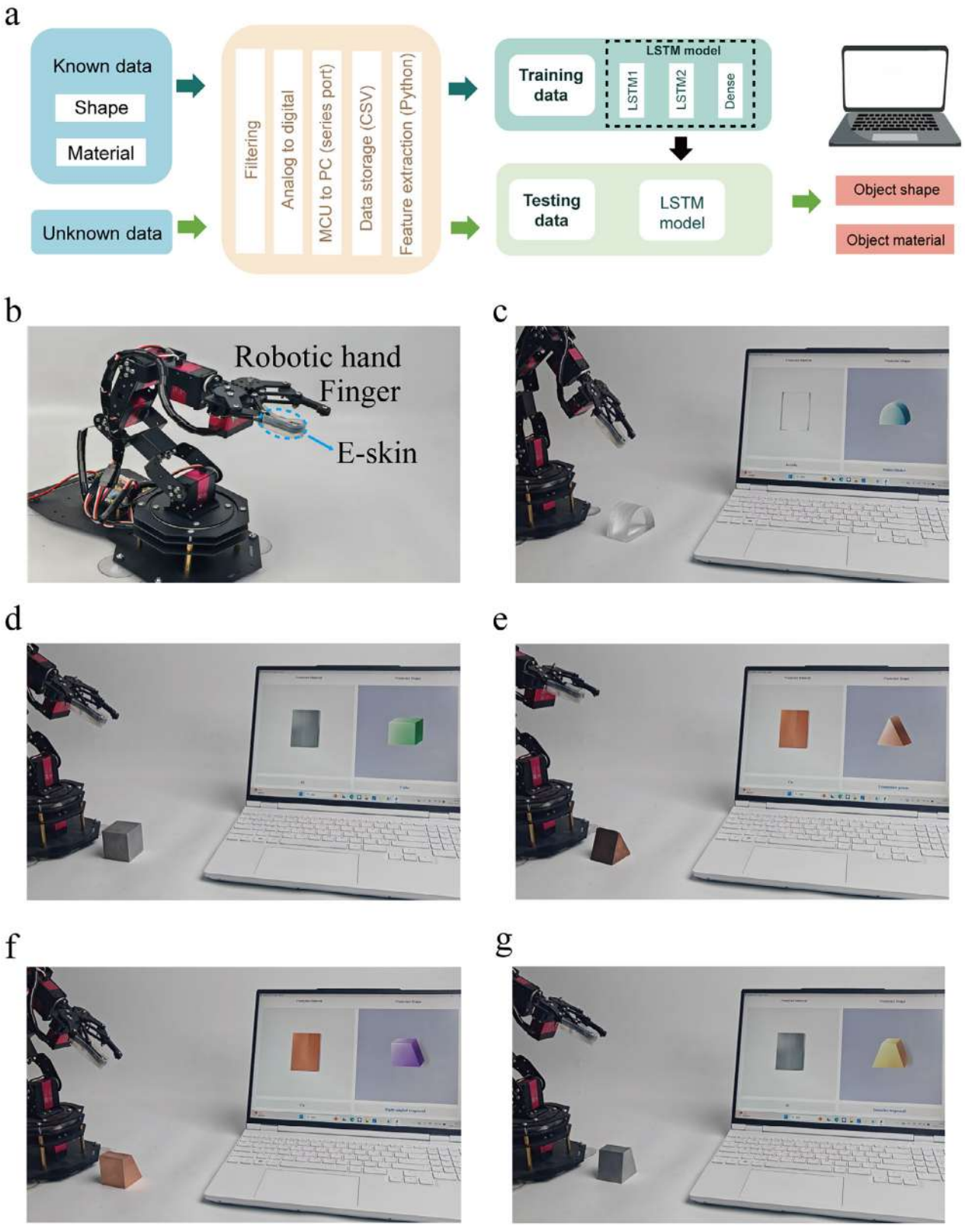

FIGURE 6 | (a) Overall computational flowchart of LSTM neural network for object shape and material identification. (b) Photography of robotic hand integrated with e-skin. (c–g) Simultaneous recognition of both shape and material: acrylic semicylinder, Al cube, Cu triangular prism, Cu right angled trapezoid and Al isosceles trapezoid.

triangular prism Cu block, right angled trapezoid Cu block, and an isosceles trapezoid Al block.

The robotic hand successfully recognized both the shape and material of each sample (Figure 6c–e; Movie S3), thereby validating the robustness and practicality of the proposed dual-mode e-skin for complex real-world perception tasks.

3 | Conclusions

A dual-mode e-skin, which offers a novel approach to non-contact sensing by leveraging the intrinsic electrostatic field generated by the embedded electret structure, was developed in this study. Compared with conventional non-contact sensing technologies, the proposed method significantly enhances the sensitivity and detection range by increasing the surface potential of the electret. Furthermore, with the assistance of an LSTM neural network, the robotic hand integrating e-skin achieved impressive accuracies of 100% and 97.35% in object-shape and object-material recognition, respectively. The e-skin provides a unique and efficient solution for multimodal perception in robotics, and enables accurate and real-time recognition of complex object attributes. This study not only introduces a new paradigm for non-contact sensing but also bridges the disparity between advanced sensing technologies and practical robotic applications, thus providing an avenue for exciting developments in intelligent robotics across various fields such as automation, healthcare, and human-robot interaction.

4 | Experimental Section

4.1 | Fabrication of E-Skin

An ePTFE membrane (50 μm thickness, average pore size of 1 μm; Changzhou Jinchun Environmental Protection Technology Co., Ltd.) was polarized using the corona charging method. A 1:1 mixture of Ecoflex 00–30 (Smooth-On Inc.) parts A and B was prepared using a mixer. The prepared elastomer solution was poured onto a charged ePTFE film and distributed evenly on a glass plate using a doctor blade. Finally, the Ecoflex precursor was solidified for 2 h at room temperature. After curing, the surface of the film was wiped with isopropanol to remove dust and grease. Meanwhile, an AgNWs dispersion solution was prepared by dispersing AgNWs in ethanol (concentration of 0.5 mg/mL), and ultrasonic treatment was conducted to prevent the agglomeration of the nanowires and ensure their uniform dispersion. The AgNWs were sprayed with a spray gun and dried naturally at room temperature.

4.2 | Characterization of the Device

The sheet resistance of the AgNWs electrode was measured by four-point probe (RG-7C, Napson Corporation, Japan). The surface potentials of the ePTFE and PTFE films were measured using a high-speed electrometer (Model-341b, Trek, America). The electrode potential was measured using a high-speed electrometer (Model-341b, Trek, America). The distance between the electronic skin and sensing object was controlled by a driving motor (PKP268D42A2-R2F, Oriental Motor, Japan) and a high-load linear stage with built-in controllers (X-LRT0500AL-E08C, Zaber Technologies, Canada).

4.3 | Statistical Analysis

Statistical analyses were performed using GraphPad Prism (version 10.6). Values are presented as the mean ± standard deviation ($n = 10$). The significance of two independent samples was calculated by the unpaired t-test (Figure 2c). When three or more samples of a single variable were involved, a one-way analysis of variance was performed (Figure 2e). Involving two variables, a two-way analysis of variance was conducted to assess the interaction between factors (Figure 3b,c). All tests were two-sided, and p-values <0.05 were considered statistically significant.

Acknowledgements

This work was financially supported by the open research fund of Suzhou Laboratory (No. SZLAB-1508-2024-ZD016).

Conflicts of Interest

The authors declare no conflicts of interest.

Data Availability Statement

The data that support the findings of this study are available from the corresponding author upon reasonable request.

References

1. I. Radosavovic, T. Xiao, B. Zhang, T. Darrell, J. Malik, and K. Sreenath, "Real-World Humanoid Locomotion with Reinforcement Learning," *Science Robotics* 9 (2024): adi9579, https://doi.org/10.1126/scirobotics.adi9579.

2. Z. He, J. Wu, J. Zhang, et al., "CDM-MPC: An Integrated Dynamic Planning and Control Framework for Bipedal Robots Jumping," *IEEE Robotics and Automation Letters* 9 (2024): 6672–6679, https://doi.org/10.1109/LRA.2024.3408487.

3. T. Haarnoja, B. Moran, G. Lever, et al., "Learning Agile Soccer Skills for a Bipedal Robot with Deep Reinforcement Learning," *Science Robotics* 9 (2024): adi8022, https://doi.org/10.1126/scirobotics.adi8022.

4. P.-H. Kuo, W.-C. Yang, P.-W. Hsu, and K.-L. Chen, "Intelligent Proximal-Policy-Optimization-Based Decision-Making System for Humanoid Robots," *Advanced Engineering Informatics* 56 (2023): 102009, https://doi.org/10.1016/j.aei.2023.102009.

5. P. Zi, K. Xu, J. Chen, et al., "Intelligent Rock-Climbing Robot Capable of Multimodal Locomotion and Hybrid Bioinspired Attachment," *Advanced Science* 11 (2024): 2309058, https://doi.org/10.1002/advs.202309058.

6. Y. Meng, Z. Bing, X. Yao, et al., "Preserving and Combining Knowledge in Robotic Lifelong Reinforcement Learning," *Nature Machine Intelligence* 7 (2025): 256–269, https://doi.org/10.1038/s42256-025-00983-2.

7. S. Luo, M. Jiang, S. Zhang, et al., "Experiment-Free Exoskeleton Assistance via Learning in Simulation," *Nature* 630 (2024): 353–359, https://doi.org/10.1038/s41586-024-07382-4.

8. Z. Shi, L. Meng, X. Shi, et al., "Morphological Engineering of Sensing Materials for Flexible Pressure Sensors and Artificial Intelligence Applications," *Nano-Micro Letters* 14 (2022): 141, https://doi.org/10.1007/s40820-022-00874-w.

9. G. Wu, X. Li, R. Bao, and C. Pan, "Innovations in Tactile Sensing: Microstructural Designs for Superior Flexible Sensor Performance,"

Advanced Functional Materials 34 (2024): 2405722, https://doi.org/10.1002/adfm.202405722.

10. L. Beker, N. Matsuhisa, I. You, et al., "A Bioinspired Stretchable Membrane-Based Compliance Sensor," *Proceedings of the National Academy of Sciences* 117 (2020): 11314–11320, https://doi.org/10.1073/pnas.1909532117.

11. Z. Liu, X. Hu, R. Bo, et al., "A Three-Dimensionally Architected Electronic Skin Mimicking human Mechanosensation," *Science* 384 (2024): 987–994, https://doi.org/10.1126/science.adk5556.

12. M. T. Flavin, K.-H. Ha, Z. Guo, et al., "Bioelastic state Recovery for Haptic Sensory Substitution," *Nature* 635 (2024): 345–352, https://doi.org/10.1038/s41586-024-08155-9.

13. F. Chen, Q. Zhuang, Y. Ding, et al., "Wet-Adaptive Electronic Skin," *Advanced Materials* 35 (2023): 2305630, https://doi.org/10.1002/adma.202305630.

14. Z. Shen, X. Zhu, C. Majidi, and G. Gu, "Cutaneous Ionogel Mechanoreceptors for Soft Machines, Physiological Sensing, and Amputee Prostheses," *Advanced Materials* 33 (2021): 2102069, https://doi.org/10.1002/adma.202102069.

15. S. Sankar, W.-Y. Cheng, J. Zhang, et al., "A Natural Biomimetic Prosthetic Hand with Neuromorphic Tactile Sensing for Precise and Compliant Grasping," *Science Advances* 11 (2025): adr9300, https://doi.org/10.1126/sciadv.adr9300.

16. L. Wang, X. Qi, C. Li, and Y. Wang, "Multifunctional Tactile Sensors for Object Recognition," *Advanced Functional Materials* 34 (2024): 2409358, https://doi.org/10.1002/adfm.202409358.

17. H. Li, H. Niu, F. Yin, W. Zhou, G. Shen, and Y. Li, "A Labor-Division Cooperation Electronic Palm System for High-Precision Crosstalk-Free Cognition of Pressure and Temperature," *Advanced Materials* (2025): e10241, https://doi.org/10.1002/adma.202510241.

18. H. Zhang, H. Li, and Y. Li, "Biomimetic Electronic Skin for Robots Aiming at Superior Dynamic-Static Perception and Material Cognition Based on Triboelectric-Piezoresistive Effects," *Nano Letters* 24 (2024): 4002–4011, https://doi.org/10.1021/acs.nanolett.4c00623.

19. S. He, J. Dai, D. Wan, et al., "Biomimetic Bimodal Haptic Perception Using Triboelectric Effect," *Science Advances* 10 (2024): ado6793, https://doi.org/10.1126/sciadv.ado6793.

20. S. Chen, J. Zhang, N. Cheng, et al., "Printing Perovskite and Graphene Parallel Structure-Based Optical-Mechanical Sensors for human-Machine Interaction," *Science China Technological Sciences* 68 (2025): 1220201, https://doi.org/10.1007/s11431-024-2816-6.

21. S. Suresh, H. Qi, T. Wu, et al., "NeuralFeels with Neural Fields: Visuotactile Perception for in-Hand Manipulation," *Science Robotics* 9 (2024): adl0628, https://doi.org/10.1126/scirobotics.adl0628.

22. Y. Liu, J. Wang, T. Liu, et al., "Triboelectric Tactile Sensor for Pressure and Temperature Sensing in High-Temperature Applications," *Nature Communications* 16 (2025): 383, https://doi.org/10.1038/s41467-024-55771-0.

23. T. W. Kang, Y. J. Lee, B. Rigo, et al., "Soft Nanomembrane Sensor-Enabled Wearable Multimodal Sensing and Feedback System for Upper-Limb Sensory Impairment Assistance," *ACS Nano* 19 (2025): 5613–5628, https://doi.org/10.1021/acsnano.4c15530.

24. A. Liang and X. Chen, "A Non-Contact Porous Composite fiber Paper-Based Humidity Sensor for Wearable Breathing and Skin Humidity Monitoring," *Journal of Materials Chemistry A* 12 (2024): 29081–29091, https://doi.org/10.1039/D4TA05393A.

25. J. Lou, Y. Yang, and C. Zhao, "Humidity Sensors Based on Octaphenylcyclotetrasiloxane Hypercrosslinked Porous Polymers for Non-Contact Sensing and respiratory Monitoring," *Sensors and Actuators B: Chemical* 421 (2024): 136478, https://doi.org/10.1016/j.snb.2024.136478.

26. F. Yin, Y. Guo, Z. Qiu, et al., "Hybrid Electronic Skin Combining Triboelectric Nanogenerator and Humidity Sensor for Contact and Non-Contact Sensing," *Nano Energy* 101 (2022): 107541, https://doi.org/10.1016/j.nanoen.2022.107541.

27. P. Sun, M. Qiu, G. Li, et al., "Artificial Jelly Channel Inspired by the Shark for Sensing Specific Ions and Environmental Perturbation," *Materials Today Chemistry* 26 (2022): 101047, https://doi.org/10.1016/j.mtchem.2022.101047.

28. Z. H. Guo, H. L. Wang, J. Shao, et al., "Bioinspired Soft Electroreceptors for Artificial Precontact Somatosensation," *Science Advances* 8 (2022): abo5201, https://doi.org/10.1126/sciadv.abo5201.

29. J. Zhou, J. Li, H. Jia, et al., "Mormyroidea-Inspired Electronic Skin for Active Non-Contact Three-Dimensional Tracking and Sensing," *Nature Communications* 15 (2024): 9875, https://doi.org/10.1038/s41467-024-54249-3.

30. E. E. Josberger, P. Hassanzadeh, Y. Deng, et al., "Proton Conductivity in Ampullae of Lorenzini Jelly," *Science Advances* 2 (2016): 1600112, https://doi.org/10.1126/sciadv.1600112.

31. X. Le, Q. Shi, Z. Sun, J. Xie, and C. Lee, "Noncontact Human–Machine Interface Using Complementary Information Fusion Based on MEMS and Triboelectric Sensors," *Advanced Science* 9 (2022): 2201056, https://doi.org/10.1002/advs.202201056.

32. Y. Tang, H. Zhou, X. Sun, et al., "Triboelectric Touch-Free Screen Sensor for Noncontact Gesture Recognizing," *Advanced Functional Materials* 30 (2020): 1907893, https://doi.org/10.1002/adfm.201907893.

33. K. Shrestha, S. Sharma, G. B. Pradhan, et al., "A Siloxene/Ecoflex Nanocomposite-Based Triboelectric Nanogenerator with Enhanced Charge Retention by MoS_2/LIG for Self-Powered Touchless Sensor Applications," *Advanced Functional Materials* 32 (2022): 2113005, https://doi.org/10.1002/adfm.202113005.

34. H. Zhou, W. Huang, Z. Xiao, et al., "Deep-Learning-Assisted Noncontact Gesture-Recognition System for Touchless Human-Machine Interfaces," *Advanced Functional Materials* 32 (2022): 2208271, https://doi.org/10.1002/adfm.202208271.

35. S. M. S. Rana, M. A. Zahed, M. T. Rahman, et al., "Cobalt-Nanoporous Carbon Functionalized Nanocomposite-Based Triboelectric Nanogenerator for Contactless and Sustainable Self-Powered Sensor Systems," *Advanced Functional Materials* 31 (2021): 2105110, https://doi.org/10.1002/adfm.202105110.

36. W. Zhang, Y. Lu, T. Liu, et al., "Spheres Multiple Physical Network-Based Triboelectric Materials for Self-Powered Contactless Sensing," *Small* 18 (2022): 2200577, https://doi.org/10.1002/smll.202200577.

37. T. Zheng, G. Li, L. Zhang, et al., "Dielectric-Enhanced, High-Sensitivity, Wide-Bandwidth, and Moisture-Resistant Noncontact Triboelectric Sensor for Vibration Signal Acquisition," *ACS Applied Materials & Interfaces* 16 (2024): 7904–7916, https://doi.org/10.1021/acsami.3c18430.

38. S. Chen, Y. Wang, L. Yang, Y. Guo, M. Wang, and K. Sun, "Flexible and Transparent Sensors with Hierarchically Micro-Nano Texture for Touchless Sensing and Controlling," *Nano Energy* 82 (2021): 105719, https://doi.org/10.1016/j.nanoen.2020.105719.

39. W. J. Song, Y. Lee, Y. Jung, et al., "Soft Artificial Electroreceptors for Noncontact Spatial Perception," *Science Advances* 7 (2021): abg9203, https://doi.org/10.1126/sciadv.abg9203.

40. Y. Liu, C. Wang, Z. Liu, et al., "Self-Encapsulated Ionic Fibers Based on Stress-Induced Adaptive Phase Transition for Non-Contact Depth-Of-Field Camouflage Sensing," *Nature Communications* 15 (2024): 663, https://doi.org/10.1038/s41467-024-44848-5.

41. R. Liu, Y. Lai, S. Li, et al., "Ultrathin, Transparent, and Robust Self-Healing Electronic Skins for Tactile and Non-Contact Sensing," *Nano Energy* 95 (2022): 107056, https://doi.org/10.1016/j.nanoen.2022.107056.

42. W. Liu, Y. Duo, X. Chen, et al., "An Intelligent Robotic System Capable of Sensing and Describing Objects Based on Bimodal, Self-Powered Flexible Sensors," *Advanced Functional Materials* 33 (2023): 2306368, https://doi.org/10.1002/adfm.202306368.

43. S. Lin, Z. Xu, S. Wang, et al., "Multiplying the Stable Electrostatic Field of Electret Based on the Heterocharge-Synergy and Superposition Effect," *Advanced Science* 9 (2022): 2203150, https://doi.org/10.1002/advs.202203150.

44. Y. Gong, K. Zhang, I. M. Lei, Y. Wang, and J. Zhong, "Advances in Piezoelectret Materials-Based Bidirectional Haptic Communication Devices," *Advanced Materials* 36 (2024): 2405308, https://doi.org/10.1002/adma.202405308.

45. J. Zhu, Y. Yang, H. Zhang, Z. Zhao, T. Hu, and L. Liu, "More than Energy Harvesting in Electret Electronics-Moving toward Next-Generation Functional System," *Advanced Functional Materials* 33 (2023): 2214859, https://doi.org/10.1002/adfm.202214859.

46. S. Zhang, Y. Wang, X. Yao, et al., "Stretchable Electrets: Nanoparticle–Elastomer Composites," *Nano Letters* 20 (2020): 4580–4587, https://doi.org/10.1021/acs.nanolett.0c01434.

47. S. Min, J. An, J. H. Lee, et al., "Wearable Blood Pressure Sensors for Cardiovascular Monitoring and Machine Learning Algorithms for Blood Pressure Estimation," *Nature Reviews Cardiology* 22 (2025): 629–648, https://doi.org/10.1038/s41569-025-01127-0.

48. K. R. Pyun, K. Kwon, M. J. Yoo, et al., "Machine-Learned Wearable Sensors for Real-Time Hand-Motion Recognition: Toward Practical Applications," *National Science Review* 11 (2023): nwad298, https://doi.org/10.1093/nsr/nwad298.

49. R. Shang, H. Chen, X. Cai, et al., "Machine Learning-Enhanced Triboelectric Sensing Application," *Advanced Materials Technologies* 9 (2024): 2301316, https://doi.org/10.1002/admt.202301316.

Supporting Information

Additional supporting information can be found online in the Supporting Information section.

Supporting File 1: adma72477-sup-0001-SuppMat.docx.

Supporting File 2: adma72477-sup-0002-MovieS1.mp4.

Supporting File 3: adma72477-sup-0003-MovieS2.mp4.

Supporting File 4: adma72477-sup-0004-MovieS3.mp4.